# Chaotic mixing in a microchannel utilizing periodically switching electro-osmotic recirculating rolls

Chih-Chang Chang and Ruey-Jen Yang*
*Department of Engineering Science, National Cheng Kung University, Tainan, Taiwan 701*
(Received 18 December 2007; published 22 May 2008)

In this study, active mixing in a microchannel with spatiotemporal variations in $\zeta$ potential distributions was investigated theoretically. In this mixing system, the primary flow is a pressure-driven flow (i.e., parabolic flow), and the electro-osmotic recirculating rolls induced by the heterogeneous $\zeta$ potential distributions act as the perturbation source. By timewise alterations of two different electro-osmotic recirculating flow fields, chaotic mixing can be induced. Blob deformation, Poincaré map, and Lyapunov exponent analyses were employed to describe the behaviors of the particle motion in this active mixing system. Finally, the optimal time-switching period was identified, which was also verified through direct numerical simulations.

DOI: 10.1103/PhysRevE.77.056311 PACS number(s): 47.52.+j, 85.85.+j

## I. INTRODUCTION

Rapid and efficient mixing is an essential but challenging task when developing microfluidic devices for chemical and biological analysis applications [1–3]. In microfluidic devices, viscous forces dominate the flow since the dimensions of such devices are very small. As a result, the flow is laminar and is restricted to the low Reynolds number regime. The mixing of two or more fluid streams in a simple microchannel is dominated by the molecular diffusion effect. The rate of diffusive mixing in microscale channels is very slow compared to the convection of the fluid along the channel since the Péclet number of typical microchannel flows is very high due to biomolecules (e.g., DNA and protein) with relatively low molecular diffusivities. Because of the low Reynolds number, it seems not possible to achieve turbulent flows (so-called Eulerian chaos) to increase the interfacial contact area over which the molecules of the two fluid streams diffuse in a simple microchannel; consequently, another approach called "chaotic advection (or so-called Lagrangian chaos)" is needed to achieve effective mixing in low Reynolds number flow regimes, which provides an effective increase in the interfacial contact area and decrease in the diffusion length [4]. A large interfacial contact area means a large area for mass transfer, while a shorter diffusion length increases the concentration gradients and increases the mass flux. In this way, the mixing time and mixing length can be considerably reduced. As the characteristic scale of the microchannel is decreased, the surface forces acting on the liquid become more significant. Therefore, surface-driven electro-osmotic flow has received significant interest as a means of controlling fluid motion in microfluidic devices in recent years [5–7]. The surface properties of the microchannel play an important role in controlling surface-driven electro-osmotic flow [7] and can be exploited to produce specific flow structures to improve the mixing performance. A number of active or passive approaches for enhanced electro-osmotic flow mixing have been proposed [3]. In this study, we will propose an active approach to cause chaotic mixing in microchannels via periodically switching electro-osmotic recirculating rolls induced by nonuniform $\zeta$ potential distributions.

According to the theory of similitude between the electro-osmotic flow velocity and the electric field [8], the electro-osmotic flow streamlines in uniform $\zeta$ potential microchannels are the same as the electric field lines governed by the electric vector field. As a result, the flow velocity and electric vector fields are both irrotational. Electro-osmotic flow fields are unique in that they can also be described as a potential flow due to the slip condition (i.e., Smoluchowski slip velocity). However, the irrotational feature of potential flow implies that closed streamlines and vortices are impossible to generate. The presence of a surface with non-uniform $\zeta$ potential is one way to produce vortices or specific flow structures in electro-osmotic flow fields. Anderson and Idol [9], Ajdari [10,11], and Stroock *et al.* [12] have performed theoretical and experimental investigations into electro-osmotic flows induced by a nonuniformly distributed $\zeta$ potential along the capillary or microchannel walls, and have suggested that the application of oppositely charged surface heterogeneities to the microchannel walls generated recirculation regions within the bulk flow. Recently, many researchers have investigated the electro-osmotic flow mixing in two-dimensional heterogeneous microchannels through numerical and experimental approaches [13–18]. The induced electro-osmotic recirculations in the two-dimensional steady flow field were successfully employed to improve species mixing in microchannels in their studies. However, the non-diffusive particles just follow the streamlines in these steady flows and, hence, chaotic mixing was absent in their proposed mixers. The mixing primarily relies on the molecular diffusion effect. Generally speaking, chaotic mixing or chaotic advection can only occur either in three-dimensional flows or time-dependent two-dimensional flows [4]. As described in the literature, electro-osmotic chaotic mixing can be induced in three-dimensional steady electro-osmotic flows with time-independent $\zeta$ potentials through the use of two-dimensional specific surface charge (or $\zeta$ potential) patterning configurations [19,20]. In addition, Wu and Liu [21] have used time-wise periodic alternations of the two-dimensional nonuniform $\zeta$ potential distributions on the bottom wall of a three-dimensional microchannel to enhance mixing. To cre-

*rjyang@mail.ncku.edu.tw

 

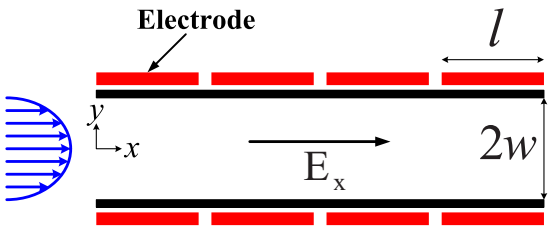


FIG. 1. (Color online). Schematic of flow mixing in a microchannel with nonuniform $\zeta$ potential distributions, which are controlled actively using a field effect.

ate electro-osmotic chaotic mixing in two-dimensional microchannels, one can spatiotemporally modulate the $\zeta$ potential distribution in a microchannel to generate an unsteady complex flow. The purpose is to get streamlines to cross at successive intervals. Qian and Bau [22] have performed theoretical studies of electro-osmotic flows in two-dimensional closed systems (i.e., zero net flow rate) driven by time-dependent $\zeta$ potentials and have demonstrated that chaotic advection can be induced by time-wise periodic alternations of the electro-osmotic recirculating rolls and can improve the mixing performance as a result, i.e., a mixing system without throughout flow. Generally, nonuniform time-dependent $\zeta$ potentials can be modulated spatiotemporally using the field effect (i.e., the so-called capacitive effect) [23,24].

In this study, we perform theoretical investigations into active mixing in a two-dimensional microchannel using spatiotemporal modulation of electro-osmotic recirculating rolls (i.e., secondary electro-osmotic flow [9]) resulting from nonuniform $\zeta$ potential distributions. Unlike the studies of Qian and Bau [22], we consider a parabolic flow as primary flow (see Fig. 1) in the mixing system and the temporal alternations of the electro-osmotic recirculating rolls act as the perturbation sources, i.e., a mixing system with continuous throughput flow (open flow system). The $\zeta$ potential distributions are modulated spatiotemporally using the field effect [24] and result in different electro-osmotic recirculating flow patterns to enhance mixing in a microchannel. In this system, the effects of the amplitude of perturbation source, time-switching period, and embedded electrode length on the mixing are considered (note that the perturbation amplitude and embedded electrode length effects on the mixing were not considered in the closed flow mixing system proposed by Qian and Bau [22]). Dynamic system techniques such as Poincare map and Lyapunov exponent analyses are then employed to investigate the mixing system. The results show these effects on the mixing are significant in the open flow mixing system. Further, the optimal time-switching period ($T_{\text{opt}}$) and Strouhal number [$\text{St}_{\text{opt}}=f_{\text{opt}}l/u_{Pm}$, where $f_{\text{opt}}=1/T_{\text{opt}}$, $l$ is the embedded electrode length, and $u_{Pm}$ is the maximum velocity (or centerline velocity) of pressure-driven flow] for mixing enhancement in this system are identified.

In Sec. II, the governing equations, analytical solutions, assumptions for this problem, mapping of the Poincaré map, and calculation of Lyapunov exponent are addressed, respectively. In Sec. III, a chaotic behavior analysis is employed to characterize the mixing and the optimal operating conditions are identified, which are also verified through the direct numerical simulation. Section IV is devoted to concluding remarks.

## II. FORMULATION

### A. Governing equations

We consider mixing in a microchannel with high aspect ratio (i.e., channel height is much larger than channel width) in our work. The effect of top and bottom walls on the flow field is assumed to be negligible and the flow field is two dimensional. Furthermore, the Reynolds number usually is smaller than unity in microfluidics, and the flow can be regarded as creeping flow or Stokes flow. Then, the combined pressure-driven and electro-osmotic flow can be described by the modified Stokes equation including an electrical body force term (i.e., Coulombic force) [25] and the continuity equation, which are given by

$$0 = -\nabla p + \mu\nabla^2\mathbf{u} + \rho_e\mathbf{E}, \tag{1}$$

$$\nabla\cdot\mathbf{u} = 0, \tag{2}$$

where $\mu$, $p$, and $\mathbf{u}$ are the fluid viscosity, pressure and flow velocity vector ($\mathbf{u}=u\hat{\mathbf{x}}+v\hat{\mathbf{y}}$), respectively. Note that the total velocity can be represented by $\mathbf{u}=\mathbf{u}_P+\mathbf{u}_{\text{EO}}$ based on the principle of superposition since Eq. (1) is linear, where $\mathbf{u}_P$ and $\mathbf{u}_{\text{EO}}$ are the velocities of pressure-driven and electro-osmotic flow, respectively. $\mathbf{E}$ is the external electric field ($\mathbf{E}=E_x\hat{\mathbf{x}}+E_y\hat{\mathbf{y}}$) and $\rho_e$ is the net charge density. Adopting the symmetric electrolyte solution and the Debye-Hückel approximation [25], the net charge density can be represented by $\rho_e=-\epsilon_r\epsilon_0\kappa^2\phi$, where $\kappa$ is termed the Debye-Hückel parameter, $\epsilon_r$ is the relative permittivity, and $\epsilon_0$ is the permittivity of vacuum. $\phi$ is the electrical double layer (EDL) potential, which can be described by the following Poisson equation [25]:

$$\nabla^2\phi = \kappa^2\phi. \tag{3}$$

For a two-dimensional incompressible flow and electrostatic field ($\nabla\times\mathbf{E}=0$), the flow can be described by

$$\mu\nabla^4\psi = -\mathbf{E}\times\nabla\rho_e, \tag{4}$$

where $\psi$ is stream function. Since $E_y=0$ within microchannels in the current study, Eq. (4) is reduced to the following equation:

$$\nabla^4\phi = \frac{\epsilon_r\epsilon_0\kappa^2E_x}{\mu}\frac{\partial\varphi}{\partial y}. \tag{5}$$

Since the stream function can be represented by $\psi=\psi_P+\psi_{\text{EO}}$ based on the principle of superposition, Eq. (5) can be decomposed into Eqs. (6) and (7),

$$\nabla^4\psi_P = 0, \tag{6}$$

$$\nabla^4\psi_{\text{EO}} = \frac{\epsilon_r\epsilon_0\kappa^2E_x}{\mu}\frac{\partial\phi}{\partial y}. \tag{7}$$

We introduce the following nondimensional parameters:

$$X=\frac{x}{w},\quad Y=\frac{y}{w},\quad \mathbf{U}=\frac{\mathbf{u}}{u_{Pm}},\quad \Psi=\frac{\psi}{u_{Pm}w},$$

$$\Phi = \frac{\phi}{|\zeta|_{\max}}, \quad \xi = \frac{\zeta}{|\zeta|_{\max}}, \tag{8}$$

where $w$, $u_{Pm}$, and $|\zeta|_{\max}$ are the half channel width, the maximum velocity of pressure-driven flow, and the maximum absolute value of the $\zeta$ potential, respectively. Then, Eqs. (3), (6), and (7) can be rewritten as

$$\nabla^2\Phi = K^2\Phi, \tag{9}$$

$$\nabla^4\Psi_P = 0, \tag{10}$$

$$\nabla^4\Psi_{\mathrm{EO}} = \Gamma K^2 \frac{\partial\Phi}{\partial Y}, \tag{11}$$

where $K=\kappa w$ is the dimensionless Debye-Hückel parameter and $\Gamma=\epsilon_r\epsilon_0|\zeta|_{\max}E_x/\mu/u_{Pm}$ is called the velocity ratio of electro-osmotic to pressure-driven flow, or the so-called amplitude of the perturbation source in this study.

### B. Analytical solutions

#### 1. Primary flow

In this study, we consider a fully developed pressure-driven flow as a primary flow (see Fig. 1), and the solutions of this flow can be easily solved with nonslip boundary conditions, which are given by

$$\Psi_P(X,Y) = Y - \frac{1}{3}Y^3, \quad U_P(X,Y) = 1 - Y^2, \tag{12}$$

and

$$V_P(X,Y) = 0,$$

where $U_P$ and $V_P$ are the dimensionless velocities of pressure-driven flow in $x$ and $y$ directions, respectively.

#### 2. Electro-osmotic recirculating flow

Figure 2(a) shows the arrangements of the embedded electrodes and applied voltages (positive or negative) on the electrodes within one period unit of the mixing channel. We assume that the $\zeta$ potential induced by the field-effect is much larger than the original $\zeta$ potential induced by the permanent surface charge of microchannels and, thus, the former dominates $\zeta$ potential along the channel wall. In addition, the distance of the gap between two separated embedded electrodes is assumed to be much smaller than the channel width ($2w$) and the electrode length ($l$). Therefore, the $\zeta$ potential distribution along the channel wall is regarded as a square wavelike periodic form. The dimensionless induced $\zeta$ potential distribution along the channel wall is given below

$$\xi(X) = \sum_{n=1}^{\infty} \frac{2}{n\pi}[1-(-1)^n]\sin(k_nX), \tag{13}$$

where $k_n=n\pi/L$ and $L=l/w$. The analytical solutions of the EDL potential corresponding to cases "A" (antisymmetric) and "B" (symmetric) [see Fig. 2(a)] can be easily obtained via Eq. (9), and are given by, respectively,

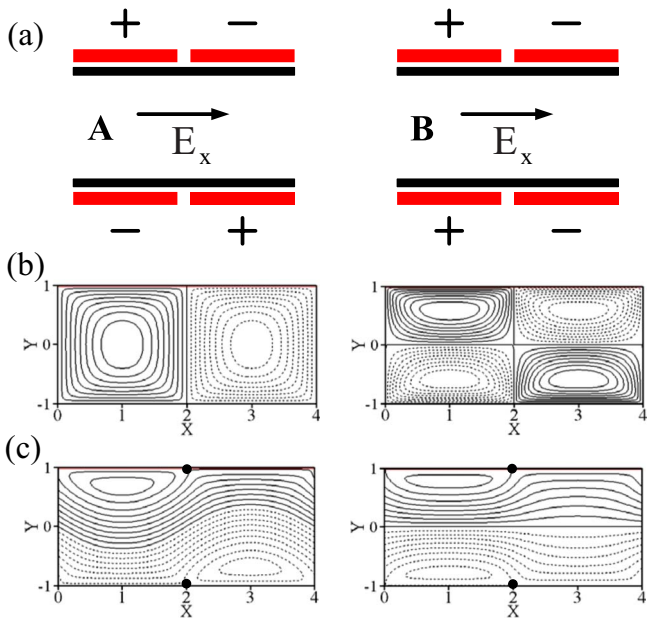


FIG. 2. (Color online). (a) The arrangements of the embedded electrodes and applied voltages (positive or negative) on the electrodes within one period unit of the mixing channel. (b) Electro-osmotic recirculating flow patterns resulting from two different spatial $\zeta$ potential distributions within one period unit of the mixing channel. (c) Total flow patterns of pressure-driven and electro-osmotic recirculating flows. Note that the symbols + and − refer to the positive and negative voltage that is applied on the embedded electrodes, respectively. The "solid" streamline refers to the counter-clockwise recirculating rolls and the "dashed" stream line refers to clockwise ones. The symbol "●" in (c) refers to the stagnation points. Here $K=500$, $\Gamma=1.0$, and $L=2.0$.

$$\Phi_A(X,Y) = \sum_{n=1}^{\infty} \frac{2}{n\pi}[1-(-1)^n]\sin(k_nX)\frac{\sinh(\alpha_nY)}{\sinh(\alpha_n)}, \tag{14a}$$

$$\Phi_B(X,Y) = \sum_{n=1}^{\infty} \frac{2}{n\pi}[1-(-1)^n]\sin(k_nX)\frac{\cosh(\alpha_nY)}{\cosh(\alpha_n)}, \tag{14b}$$

where $\alpha_n=(k_n^2+K^2)^{1/2}$.

Upon substituting Eqs. (14a) and (14b) into Eq. (11), respectively, the electro-osmotic flow fields "A" and "B" can be solved with the nonslip boundary condition and the following boundary conditions, i.e.,

$$\Psi_{\mathrm{EO}}(x,1) = Q_{\mathrm{EO}} \quad \text{and} \quad \Psi_{\mathrm{EO}}(x,-1) = 0, \tag{15}$$

where $Q_{\mathrm{EO}}$ is the dimensionless flow rate of electro-osmotic flow. From Eq. (13), we know that the effective $\zeta$ potential along the channel wall within one period unit is zero and, thus, the net flow rate of the electro-osmotic flow is zero, i.e., $Q_{\mathrm{EO}}=0$ in this study. The analytical solutions of the electroosmotic flow fields "A" and "B" are given by Eqs. (16a)–(16e) and (17a)–(17e), respectively,

$$\Psi_{\mathrm{EO}\ A}(X,Y) = \Gamma \sum_{n=1}^{\infty} \frac{2}{n\pi}[1-(-1)^n]\sin(k_n X)\left[A_n \cosh(k_n Y) + D_n Y \sinh(k_n Y) + \frac{\alpha_n}{K^2}\frac{\cosh(\alpha_n Y)}{\sinh(\alpha_n)}\right], \tag{16a}$$

$$U_{\mathrm{EO}\ A}(X,Y) = \Gamma \sum_{n=1}^{\infty} \frac{2}{n\pi}[1-(-1)^n]\sin(k_n X)\left\{A_n k_n \sinh(k_n Y) + D_n[\sinh(k_n Y) + k_n Y \cosh(k_n Y)] + \frac{\alpha_n^2}{K^2}\frac{\sinh(\alpha_n Y)}{\sinh(\alpha_n)}\right\}, \tag{16b}$$

$$V_{\mathrm{EO}\ A}(X,Y) = -\Gamma \sum_{n=1}^{\infty} \frac{2}{n\pi}[1-(-1)^n]k_n \cos(k_n X)\left[A_n \cosh(k_n Y) + D_n Y \sinh(k_n Y) + \frac{\alpha_n}{K^2}\frac{\cosh(\alpha_n)}{\sinh(\alpha_n)}\right], \tag{16c}$$

where

$$A_n = -\frac{\alpha_n[k_n \cosh(k_n)\coth(\alpha_n) + \sinh(k_n)\coth(\alpha_n) - \alpha_n \sinh(k_n)]}{K^2[\cosh(k_n)\sinh(k_n) + k_n]}, \tag{16d}$$

$$D_n = -\frac{\alpha_n[\alpha_n \cosh(k_n) - k_n \sinh(k_n)\coth(\alpha_n)]}{K^2[\cosh(k_n)\sinh(k_n) + k_n]}, \tag{16e}$$

$$\Psi_{\mathrm{EO}\ B}(X,Y) = \Gamma \sum_{n=1}^{\infty} \frac{2}{n\pi}[1-(-1)^n]\sin(k_n X)\left[B_n \sinh(k_n Y) + C_n Y \cosh(k_n Y) + \frac{\alpha_n}{K^2}\frac{\sinh(\alpha_n Y)}{\cosh(\alpha_n)}\right], \tag{17a}$$

$$U_{\mathrm{EO}\ B}(X,Y) = \Gamma \sum_{n=1}^{\infty} \frac{2}{n\pi}[1-(-1)^n]\sin(k_n X)\left\{B_n k_n \cosh(k_n Y) + C_n[\cosh(k_n Y) + k_n Y \sinh(k_n Y)] + \frac{\alpha_n^2}{K^2}\frac{\cosh(\alpha_n Y)}{\cosh(\alpha_n)}\right\}, \tag{17b}$$

$$V_{\mathrm{EO}\ B}(X,Y) = -\Gamma \sum_{n=1}^{\infty} \frac{2}{n\pi}[1-(-1)^n]k_n \cos(k_n X)\left[B_n \sinh(k_n Y) + C_n Y \cosh(k_n Y) + \frac{\alpha_n}{K^2}\frac{\sinh(\alpha_n Y)}{\cosh(\alpha_n)}\right], \tag{17c}$$

where

$$B_n = -\frac{\alpha_n[k_n \sinh(k_n)\tanh(\alpha_n) + \cosh(k_n)\tanh(\alpha_n) - \alpha_n \cosh(k_n)]}{K^2[\cosh(k_n)\sinh(k_n) - k_n]}, \tag{17d}$$

$$C_n = -\frac{\alpha_n[\alpha_n \sinh(k_n) - k_n \cosh(k_n)\tanh(\alpha_n)]}{K^2[\cosh(k_n)\sinh(k_n) - k_n]}. \tag{17e}$$

### C. Important time scales for quasi-steady Stokes flow assumption in our analysis

Two time scales should be considered for the case of the temporal $\zeta$ potential induced by the field effect. One is the charge relaxation time for the EDL capacitor, which is generally less than several microseconds when the EDL thickness is thin ($\sim\lambda_D^2/D_i$, where $\lambda_D$ is the Debye length [25] and $D_i$ is the diffusivity of ions). Another is the time required for fully charging the capacitor of the wall (i.e., RC time or charge relaxation time). The charge relaxation time for the Pyrex 7740 / soda-lime glass is on the order of $10^{-2}$ s. The time-switching period of the applied voltage on the embedded electrodes in this study is usually much larger than the two charge relaxation time scales, and the value of the temporal $\zeta$ potential can be regarded as a quasisteady value. In addition, the time-switching period is also much larger than the time scale of viscous diffusion ($\sim w^2/\nu$) in our work (i.e., the dimensionless time-switching period $T \gg \mathrm{Re}$, where $\mathrm{Re} = u_{Pm} w/\nu$, $\mathrm{Re} < 0.1$ in the current study). Consequently, the time-dependent flows can be regarded as quasisteady Stokes flows.

### D. Particle tracing algorithm and characterization of chaotic mixing

We adopt the particle tracing algorithm to investigate the dynamic behaviors of the mixing in this study. The motion of a passive tracer can be governed by the following kinematic equation:

$$\frac{d\mathbf{X}}{d\tau} = g_A(\tau)\mathbf{U}_A(X,Y) + g_B(\tau)\mathbf{U}_B(X,Y), \tag{18}$$

where

$$g_A(\tau) = \begin{cases} 1, & (k-1)T < \tau < (2k-1)T/2 \\ 0, & (2k-1)T/2 < \tau < kT \end{cases},$$

$$g_B(\tau) = \begin{cases} 0, & (k-1)T < \tau < (2k-1)T/2 \\ 1, & (2k-1)T/2 < \tau < kT \end{cases},$$

$\mathbf{X}$ is the location of the tracer particle, the dimensionless time $\tau = t/w/u_{Pm}$, the dimensionless time period $T = T/w/u_{Pm}$, and the number of time periods $k = 1, 2, 3, \ldots$. Note that $\mathbf{U}_A = \mathbf{U}_P + \mathbf{U}_{EO\ A}$ and $\mathbf{U}_B = \mathbf{U}_P + \mathbf{U}_{EO\ B}$. The fourth-order Runge-Kutta method with a fixed time step is employed to integrate Eq. (18).

In order to understand and optimize fluid deformation during the mixing process, it is necessary to understand the mechanisms of fluid stretching and folding and evaluate them in a quantitative manner. In the past two decades, it has been demonstrated that chaotic mixing is associated with the stretching and folding of fluid elements as described by dynamic system techniques [4]. In this study, we adopt both of the Poincaré map and Lyapunov exponent analyses to describe the mixing system. Poincaré maps can be used to explain the mixing process of the system as the system goes from periodic to chaotic. A Poincaré map analysis is commonly used to simplify the analysis of an $n$-dimensional dynamic system by reducing it to $n-1$ dimensions. For the active mixing scheme, the Poincaré map can be applied by setting an appropriate mapping. For the trajectory of any initial point, we choose the Poincaré section in time to be $\tau_k = k \times \mathrm{T}$, and the number of time periods $k = 1, 2, 3, \ldots$. The trajectory will intersect these planes successively at locations $\mathbf{X}_1, \mathbf{X}_2, \ldots, \mathbf{X}_k$ and define a mapping $\mathbf{X}_{k+1} = f(\mathbf{X}_k)$. Note that $X_k = \mathrm{mod}(X_k, 2L)$. Lyapunov exponent, as the average exponential rates of divergence or convergence of nearby orbits in the phase space, can describe chaos in a quantitative manner and then provide information on the effects of the parameters such as the amplitude and frequency of perturbation source as the system goes chaotic. The infinite-time Lyapunov exponent ($\lambda$) is expressed as Eq. (19), which is given by

$$\lambda = \lim_{\tau \to \infty} \lim_{|d\mathbf{X}_0| \to 0} \frac{1}{\tau} \ln \left[ \frac{|d\mathbf{X}(\tau)|}{|d\mathbf{X}_0|} \right], \tag{19}$$

where $|d\mathbf{X}_0|$ and $|d\mathbf{X}(\tau)|$ are the distance between two particles at initial condition and time $\tau$, respectively. This study adopts Sprott's method to calculate the value of the infinite-time Lyapunov exponent (i.e., largest Lyapunov exponent) [26]. A positive Lyapunov exponent indicates chaos.

## III. RESULTS AND DISCUSSIONS

Figure 2(b) reveals the electro-osmotic flow patterns "A" and "B" within one period unit of the mixing channel (i.e., $2L$) calculated from Eqs. (16a) and (17a), respectively. The fluid flows in the opposite direction of the external electric field in the positively charged walls due to excess negative ions in the diffuse layer move opposite to the electric field direction, while the fluid flows in the same direction as the electric field in negatively charged walls. To satisfy the continuity condition, the recirculating flows are then produced, which act as a perturbation source in this active mixing scheme. The total flow patterns (i.e., combination of pressure-driven and electro-osmotic recirculating flows) for flow fields A and B are shown in Fig. 2(c), respectively. It can be seen clearly that the stagnation points exist at the location $(mL, \pm 1)$, where $L = 2.0$ and $m = 1, 2, 3\ldots$. The stagnation point is similar to the saddle point referred to in the mathematical definition of bifurcation in a dynamic system [26], which plays an important role in achieving chaotic mixing. The stretching rate near these points is much higher than that of shear flow [27]. In addition, the recirculating rolls may fold the fluid element. By periodically switching flow fields A and B ($\mathbf{U}_A$ and $\mathbf{U}_B$), the chaotic mixing can be induced under the appropriate operating conditions.

### A. Dynamic analysis

Figure 3 shows the Poincaré maps corresponding to the different time periods with an amplitude of $\Gamma = 1.0$. Lines and white regions are revealed in the Poincaré maps. The lines represented particles continued to move in ordered trajectories. The white region is isolated due to the presence of KAM curves. It could be a single ordered region, or it could contain both ordered and chaotic regions. The KAM curves separate the ordered region from the chaotic region [4]. Any trajectory of a point initiated in one attractor (quasiperiodic area or chaotic area) cannot cross over the KAM curves to another attractor. In other words, the KAM curves act as boundaries that prevent the mixing of fluid elements between the two types of regions without considering the molecular diffusion effect. In the case of $T = 1.0$, the major portion of the particles continued to move in ordered trajectories, as indicated by the presence of lines. Only particles close to the channel wall ($Y = -1.0$) become locally chaotic. These lines break up as the time period is increased. When $T = 4.0$ and $T = 5.0$, the results show the size of the chaotic regions is large compared to the other time periods. Although the lines seem to break up and result in chaotic behavior in the cases of $T = 2.0$ and $T = 8.0$, there are periodiclike lines (KAM curves) close to the interface line acting as a barrier that separates the blue and red chaotic regions. The periodiclike line prevents any exchanges between the two regions, and results in a poor mixing compared to the cases of $T = 4.0$ and $T = 5.0$ in Fig. 3 even for those particles moving in a chaotic manner. In the Poincaré maps analysis, we found that the size of the white region isolated by the KAM curves is the smallest when the time-switching period is around $T = 4.0$ for most of the amplitudes ($\Gamma$).

Poincaré maps provide schematic illustrations on chaos. Lyapunov exponent can describe the stretching rate of a fluid element in a quantitative manner. Combination of both Poincaré maps and Lyapunov exponent, therefore, can be employed to measure and analyze the relationships of different operating conditions with chaos. To investigate the effect of the amplitude ($\Gamma$) and time-switching period ($T$) of the perturbation source to chaos, we calculate the infinite-time Lyapunov exponent (i.e., largest Lyapunov exponent) for different values of $\Gamma$ and $T$ by dividing the $(\Gamma, T)$ plane into grids to obtain Fig. 4. In the chaotic regions with a positive

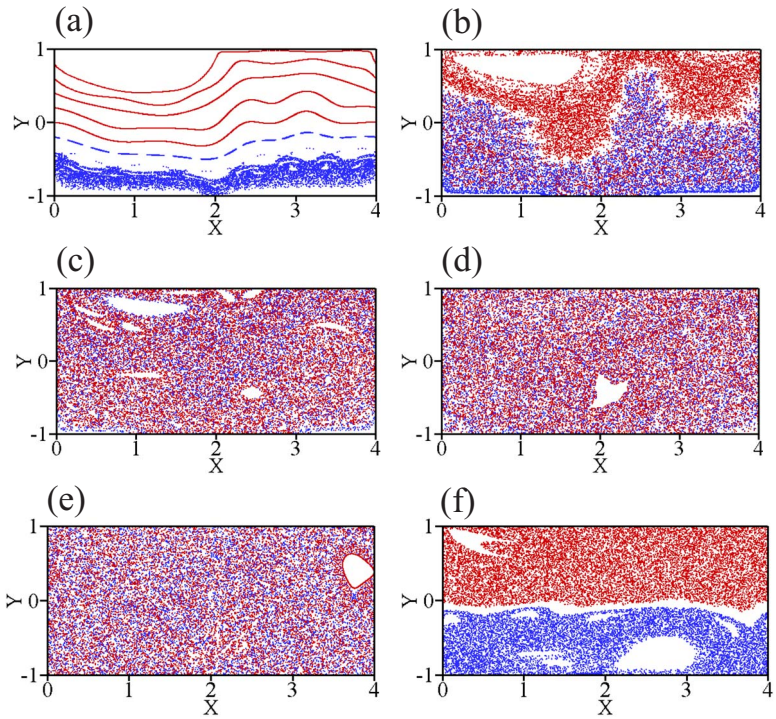


FIG. 3. (Color online). Poincaré maps for the different time periods when $\Gamma=1.0$ and $L=2.0$. (a) $T=1.0$, (b) $T=2.0$, (c) $T=3.0$, (d) $T=4.0$, (e) $T=5.0$, and (f) $T=8.0$. These figures were all mapped for 2500 time periods with nine particles, which are located at initial points $(X_0, Y_0)$ (0.0, −0.8), (0.0, −0.6), (0.0, −0.4), (0.0, −0.2), (0.0, 0.0), (0.0, 0.2), (0.0, 0.4), (0.0, 0.6), and (0.0, 0.8), respectively.

value, the Lyapunov exponent increases as $\Gamma$ increases and the larger Lyapunov exponent appears around $T=4.0$. For most of the initial positions, $T=4.0$ is the best time-switching period in the present analysis. It seems to be independent of the amplitude of the perturbation source ($\Gamma$) in the range of $0 \leq \Gamma \leq 2$. From the Poincaré maps and Lyapunov exponent analysis, the optimal time-switching period for mixing appears to be around $T=4.0$.

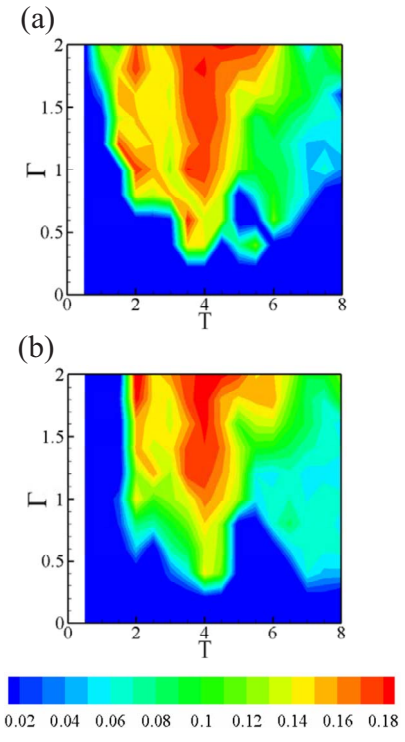


FIG. 4. (Color online). Contour plots of infinite-time Lyapunov exponents on the $(\Gamma, T)$ planes with different initial positions: (a) (0.0, 0.0) and (b) (0.0, 0.5). Here $L=2.0$.

In Fig. 5(a), the value of the Lyapunov exponent is shown to be strongly dependent on the initial position of the particle at the fixed time period $T=4.0$ when the amplitude is small. This is because the initial positions of the particles are in different attractors. From Poincaré maps in Figs. 3, we know that the trajectory of any initial position will be trapped in the attractor that the initial position lies in, whether it is a chaotic attractor or a periodic attractor. Therefore, the Lyapunov exponent should also depend on the initial positions, which is quite different from simple temporal chaotic systems such as the Lorenz attractor. As a result, the Lyapunov exponent is not the only parameter determining the effective mixing in the system when the amplitude is small or the system is not globally chaotic. However, the value of the Lyapunov exponent would be weakly dependent on the initial position of the particle when the amplitude is larger than 0.5, especially for $\Gamma > 1.0$, which implies the dynamic behavior is almost globally chaotic. Figure 5(b) shows the Lyapunov exponent of the particle located at different initial positions within one period unit of the mixing channel when $L=2.0$, $T=4.0$, and $\Gamma=1.0$. Comparing this with the Poincaré map shown in Fig. 3(d), the white island reveals the zero Lyapunov exponent region. Note that small variations in the Lyapunov exponents of the chaotic region in Fig. 5(b) are due to finite-time effects in calculating the infinite-time Lyapunov exponent. A KAM curve exists between the zero Lyapunov exponent region and the chaotic region. The size of the island is found to decrease as the amplitude $\Gamma$ increases. Using the combination of both the Poincaré maps and Lyapunov exponent analysis, we infer that the optimum mixing would be induced in the system when the time-switching period ($T$) is around 4.0 and the amplitude ($\Gamma$) is larger than 1.0. Figure 6 shows a sequence of blob deforma-

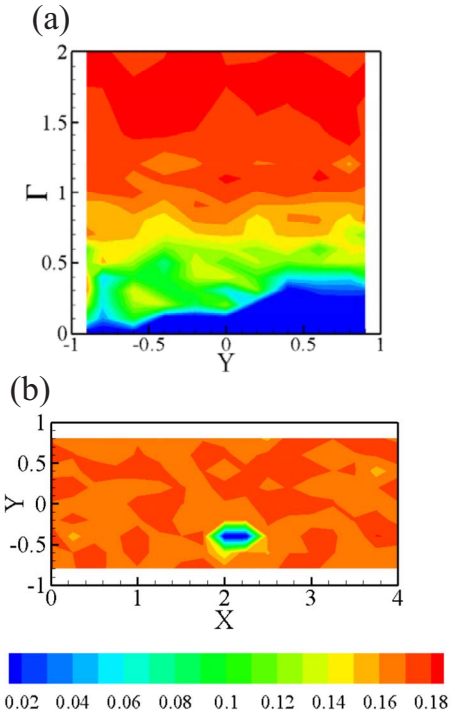


FIG. 5. (Color online). Contour plots of infinite-time Lyapunov exponents on the (a)$(\Gamma, Y)$ plane ($T$=4.0, $X_0$=0.0) and (b) $(X, Y)$ plane ($T$=4.0, $\Gamma$=1.0). Note that the $(X, Y)$ plane refers to the initial point of the particles within one period unit of the mixing channel.

tions when $T$=4.0 and $\Gamma$=2.0, which also reveals that the system is chaotic.

### B. Visualization of mixing through direct numerical simulations

To verify the above results (Poincaré map and Lyapunov exponent analysis) obtained from the particle tracing algorithm, the species mixing under the different operating conditions was visualized through direct numerical simulations [i.e., the species convection-diffusion equation was solved numerically using an alternative-direction-implicit (ADI) scheme [14]], as shown in Fig. 7. Here the Péclet number is defined as $\mathrm{Pe}=u_{Pm}w/D_s$, where $D_s$ is the species diffusivity. The results indicate that the optimal time periods for the two different amplitudes $\Gamma$=1.0 and $\Gamma$=2.0 are both 4.0, which confirms the results obtained from the Poincaré map and Lyapunov exponent analysis. It also can be seen clearly that the fluid elements were stretched and folded significantly under the appropriate operating conditions, especially for the case of $\Gamma$=2.0 and $T$=4.0. Therefore, the time and length required for complete mixing can be effectively reduced.

### C. Effect of the embedded electrode length ($L$) on the optimal time-switching period ($T$)

The above results showed that the dimensionless optimal time period $T_{\mathrm{opt}}$ is 4.0 in the case of $L$=2.0, which is weakly dependent on the amplitude of the perturbation source in the range of $0<\Gamma\leq 2.0$. We infer that the optimal time period may be dependent on the length of the embedded electrode. Furthermore, the infinite-time Lyapunov exponent analysis is also employed to find the optimal time periods for different embedded electrode lengths ($L$). From Eqs. (16b), (16c), (17b), and (17c), we know that computing the infinite-time Lyapunov exponent is a time-consuming task in the case of the square wave $\zeta$ potential distribution due to the fact that the solutions of the velocity fields are series solutions. In order to reduce the computation time, the sinusoidal wave $\zeta$ potential distribution along the channel walls is assumed to investigate the effect of the embedded electrode length on the optimal time period. In Fig. 8, it is obvious that the optimal time period is strongly dependent on the length of the embedded electrodes. In addition, the value of the Lyapunov exponent decreases as the length of the embedded electrodes is increased. In the case of $L$=2.0, the optimal time period is also shown to be weakly dependent on the amplitude ($\Gamma$), which is close to 4.0. The value of the Lyapunov exponent is smaller than that in Fig. 4 for a given operating condition. This is because the strength of the electro-osmotic recirculating rolls in the case of the sinusoidal wave $\zeta$ potential distribution is always smaller than that of the case of the square wave $\zeta$ potential distribution. The dimensionless optimal time periods are approximately 3.0, 4.0, and 6.0 for $L$=1.5, $L$=2.0, and $L$=3.0, respectively.

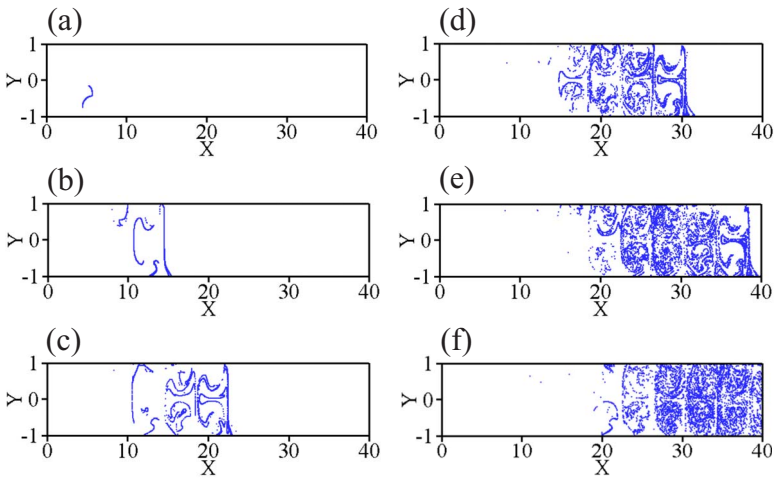


FIG. 6. (Color online). A sequence of blob deformations when $L$=2.0, $\Gamma$=2.0, and $T$=4.0. (a) $\tau$=2$T$, (b) $\tau$=4$T$, (c) $\tau$=6$T$, (d) $\tau$=8$T$, (e) $\tau$=10$T$, and (f) $\tau$=12$T$. The size of the blob is 0.1×0.1 and comprises 10000 particles, which were placed initially at location (0.05, −0.55).

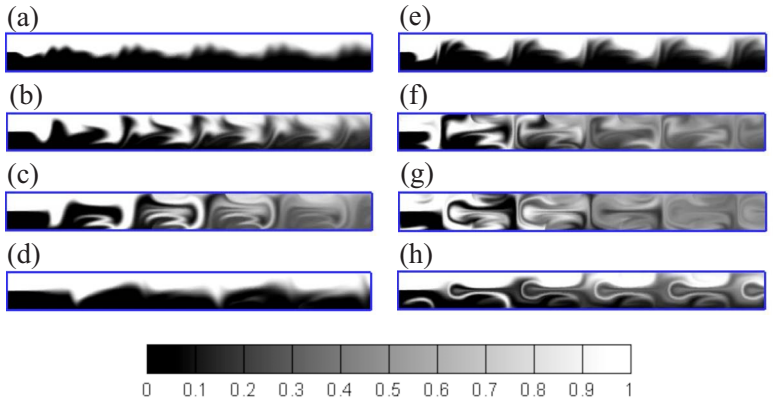


FIG. 7. (Color online) Contour plots of species concentration distribution at different operation conditions. (a) $\Gamma=1.0$, $T=1.0$, (b) $\Gamma=1.0$, $T=2.0$, (c) $\Gamma=1.0$, $T=4.0$, (d) $\Gamma=1.0$, $T=8.0$, (e) $\Gamma=2.0$, $T=1.0$, (f) $\Gamma=2.0$, $T=2.0$, (g) $\Gamma=2.0$, $T=4.0$, and (h) $\Gamma=2.0$, $T=8.0$. Note that the Péclet number Pe=1000, the mixing length is 10 times the width of the channel, and $L=2.0$.

However, the dimensionless optimal time period also seems dependent on the amplitude when $L>3.0$ and $\Gamma>1.0$.

Furthermore, we infer that the optimal time period is approximately $T_{\text{opt}}\approx 2t_c$, where $t_c$ is defined as the time required for the particle to travel across the half-length of one period unit of the mixing channel (i.e., $l$). The time can be roughly scaled by $l/u_{Pm}$ if $t_c$ weakly depends on the amplitude of the perturbation source. In other words, the dimensionless optimal time period is $T_{\text{opt}}\approx 2L/U_{Pm}$, where $U_{Pm}=1.0$. This can be explained by the stagnation point effect on chaotic mixing in this active mixing system [stagnation points exist at the positions $(mL,\pm 1)$, $m=1,2,3,\ldots$]. Recalling the flow fields shown in Fig. 2(c), we imagine that the fluid element near the inlet is first transported to $L$ in the $x$ coordinate during the first half of the time period (flow field A), and then flow field B pushes it to the region near the stagnation points during the second half of the time period. This working process will result in the largest stretching rate. Note that the stagnation point usually plays an important role for fluid element stretching, while the recirculating roll plays an important role for fluid element folding in this mixing system. From the definition of the Lyapunov exponent, we know that the value of the Lyapunov exponent (i.e., stretching rate) decreases as the time $t_c$ increases, which confirms the results presented in Fig. 8. The dimensionless time $(\tau_c)$ required for a particle to travel from the position (0.0, 0.0) to $L$ in the $x$ coordinate during the first half time period (flow field A) can be obtained from the following equations:

$$L=\int_0^{\tau_c} U_A(X,Y)d\tau, \tag{20a}$$

$$Y_L=\int_0^{\tau_c} V_A(X,Y)d\tau, \tag{20b}$$

where $Y_L$ is the particle position in the $y$ coordinate when the particle reaches the $x$ coordinate $(L)$. Equations (20a) and (20b) are solved numerically together. The dimensionless particle travel time $\tau_c$ for the different amplitudes and embedded electrode lengths are shown in Fig. 9. It can be obviously seen that the particle travel time is slightly dependent on the amplitude $\Gamma$ in the cases of $1.5\leq L\leq 3.0$ and $0.0<\Gamma\leq 2.0$. However, it may be strongly dependent on the amplitude when $\Gamma>2.0$. In the cases of $L>3.0$, the dimensionless particle travel time decreases significantly as the am-

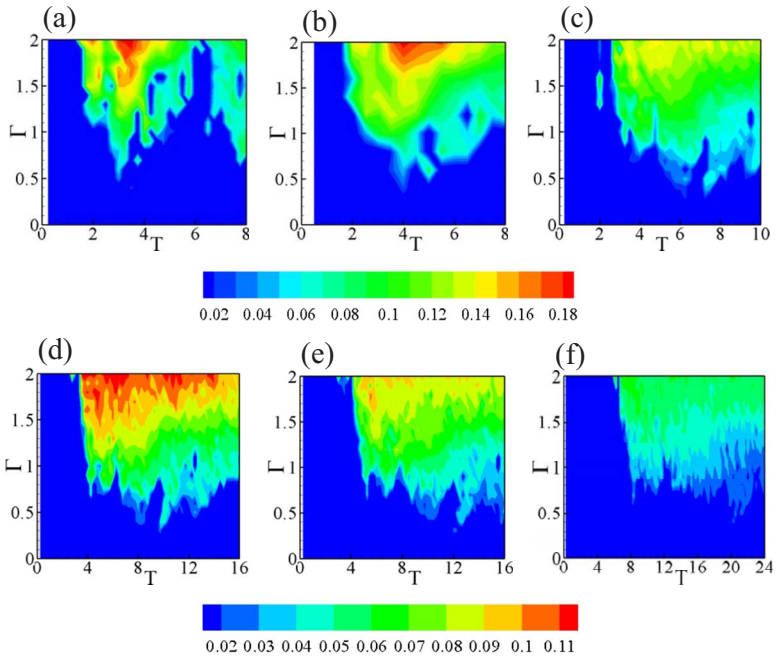


FIG. 8. (Color online) Contour plots of infinite-time Lyapunov exponents on the $(\Gamma,T)$ planes for the different embedded electrode lengths. (a) $L=1.5$, (b) $L=2.0$, (c) $L=3.0$, (d) $L=4.0$, (e) $L=5.0$, and (f) $L=8.0$. Note the differences in the color code for the top and bottom panels. The initial position of the particle is (0.0, 0.0) and the spatial $\zeta$ potential distribution is assumed to be a form of sinusoidal wave.

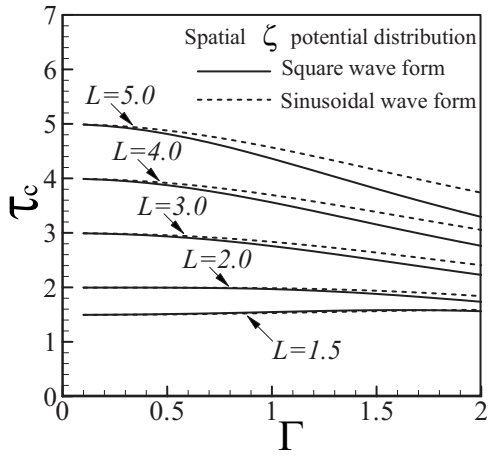


FIG. 9. The time required for a particle to travel from (0.0, 0.0) to $(L, Y_L)$ as a function of the amplitude ($\Gamma$) for the different dimensionless embedded electrode lengths ($L$).

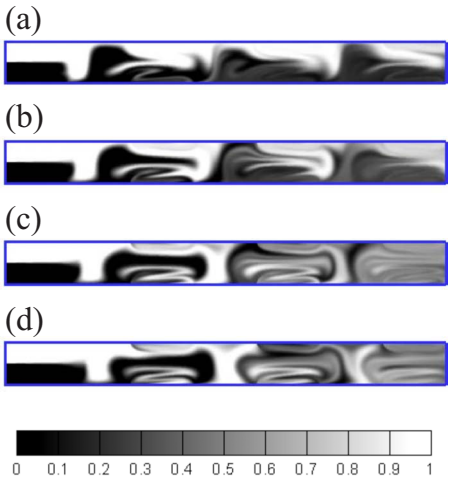


FIG. 10. (Color online) Contour plots of species concentration distribution at different time periods when $L=3.0$. (a) $T=4.0$, (b) $T=5.0$, (c) $T=6.0$, and (d) $T=7.0$. Here $\Gamma=1.0$ and $\mathrm{Pe}=1000$.

plitude is increased when $\Gamma > 1.0$. We infer that the dimensionless optimal time period $T_{\mathrm{opt}}$ decreases as the amplitude is increased in the cases of $L=4.0$ and $L=5.0$, which confirms the Lyapunov exponent computation results of the case of $L \geq 4.0$ shown in Fig. 8. Figure 10 reveals that the dimensionless optimal time periods for $L=3.0$ is approximately 6.0 at the amplitude of $\Gamma=1.0$, which is shown to be consistent with the scaling expression $T_{\mathrm{opt}} \approx 2\tau_c$. Note that $\tau_c$ for the case of $L=3.0$ is 2.8 at an amplitude of $\Gamma=1.0$.

Finally, we conclude that the dimensionless optimal time period is $T_{\mathrm{opt}} \approx 2\tau_c$. The scaling expression can be simplified to be $T_{\mathrm{opt}} \approx 2L$ when $\tau_c$ is weakly dependent on the amplitude $\Gamma$, e.g., in the ranges of $1.5 \leq L \leq 3.0$ and $0.0 < \Gamma \leq 2.0$. Then, the optimal Strouhal number is defined as $\mathrm{St}_{\mathrm{opt}} = f_{\mathrm{opt}}(2l)/u_{Pm} = 1.0$, where $f_{\mathrm{opt}} = 1/T_{\mathrm{opt}}$.

## IV. CONCLUDING REMARKS

The Poincaré map and infinite-time Lyapunov exponent analysis both have been employed to investigate the chaotic mixing induced by periodically switching the electro-osmotic recirculating rolls in two-dimensional microchannels. The electro-osmotic recirculating rolls were created by patterning nonuniform $\zeta$ potential distributions in microchannels, which are spatiotemporally modulated using the field effect. We found that the Lyapunov exponent increases as the amplitude of perturbation source is increased but decreases as the embedded electrode length is increased. The dimensionless optimal time period was found to be approximately $T_{\mathrm{opt}} \approx 2\tau_c$. When the particle travel time $\tau_c$ is slightly dependent on the amplitude of the perturbation source ($\Gamma$), the dimensionless optimal time period was simplified to be $T_{\mathrm{opt}} \approx 2L$. Then, the optimal Strouhal number $\mathrm{St}_{\mathrm{opt}} = f_{\mathrm{opt}}(2l)/u_{Pm}$ is approximately 1.0. In microfluidics, the channel dimensions are typically of the order of several hundreds micrometers, and the flow velocities typically are of the order of several hundreds of micrometers per second. This implies that the active mixing system usually works at low frequency. For example, if the primary flow velocity is $u_p = 200$ $\mu$m/s and the embedded electrode length is $l = 100$ $\mu$m, the optimal time period is approximately $f_{\mathrm{opt}} \approx 1$ Hz. In addition, the $\zeta$ potential dominated by the permanent surface charge of the microchannel may not be much smaller than the field-effect induced $\zeta$ potential and should be considered. Hence, the homogeneous surface-driven electro-osmotic flow (pluglike flow), instead of pressure-driven flow, acts as the primary flow, and could also be investigated in the future. As such, this active flow mixing system is entirely driven by electro-osmosis.

## ACKNOWLEDGMENTS

The authors gratefully acknowledge the financial support provided to this study by the National Science Council of Taiwan under Grant Nos. NSC 95-2212-E-006-253 and NSC-95-2221-E −006-384-MY2.

[1] H. A. Stone, A. D. Stroock, and A. Ajdari, Annu. Rev. Fluid Mech. **36**, 381 (2004).
[2] N.-T. Nguyen and Z. Wu, J. Micromech. Microeng. **15**, R1 (2005).
[3] C.-C. Chang and R.-J. Yang, Microfluid. Nanofluid. **3**, 501 (2007).
[4] J. M. Ottino, *The Kinematics of Mixing: Stretching, Chaos, and Transport* (Cambridge University Press, Cambridge, 1989).
[5] D. Li, *Electrokinetics in Microfluidics* (Elsevier Academic Press, Amsterdam, 2004).
[6] H.-C. Chang, Can. J. Chem. Eng. **84**, 146 (2006).

[7] A. D. Stroock and G. M. Whitesides, Acc. Chem. Res. **36**, 597 (2003).
[8] E. B. Cummings, S. K. Griffiths, R. H. Nilson, and P. H. Paul, Anal. Chem. **72**, 2526 (2000).
[9] J. L. Anderson and W. K. Idol, Chem. Eng. Comm. **38**, 93 (1985).
[10] A. Ajdari, Phys. Rev. Lett. **75**, 755 (1995).
[11] A. Ajdari, Phys. Rev. E **53**, 4996 (1996).
[12] A. D. Stroock, M. Weck, D. T. Chiu, W. T. S. Huck, P. J. A. Kenis, R. F. Ismagilov, and G. M. Whitesides, Phys. Rev. Lett. **84**, 3314 (2000).
[13] D. Erickson and D. Li, Langmuir **18**, 1883 (2002).
[14] C.-C. Chang and R.-J. Yang, J. Micromech. Microeng. **14**, 550 (2004).
[15] F. Tian, B. Li, and D. Y. Kwok, Langmuir **21**, 1126 (2005).
[16] G. H. Tang, Z. Li, J. K. Wang, Y. L. He, and W. Q. Tao, J. Appl. Phys. **100**, 094908 (2006).
[17] J.-B. Zhang, G. W. He, and F. Liu, Phys. Rev. E **73**, 056305 (2006).
[18] J.-L. Lin, G.-B. Lee, and K.-H. Lee, J. Micromech. Microeng. **16**, 757 (2006).
[19] E. Biddiss, D. Erickson, and D. Li, Anal. Chem. **76**, 3208 (2004).
[20] C.-C. Chang and R.-J. Yang, J. Micromech. Microeng. **16**, 1453 (2006).
[21] H.-Y. Wu and C.-H. Liu, Sens. Actuators, A **118**, 107 (2005).
[22] S. Qian and H. H. Bau, Anal. Chem. **74**, 3616 (2002).
[23] C. S. Lee, D. McManigill, C. T. Wu, and B. Patel, Anal. Chem. **63**, 1519 (1991).
[24] R. B. M. Schasfoort, S. Schlautmann, J. Hendrikse, and A. Van den Berg, Science **286**, 942 (1999).
[25] R. F. Probstein, *Physicochemical Hydrodynamics: An Introduction* (John Wiley & Sons, New York, 1994).
[26] J. C. Sprott, *Chaos and Time-Series Analysis* (Oxford University Press, Oxford, 2003).
[27] S. Wiggins and J. M. Ottino, Philos. Trans. R. Soc. London, Ser. A **362**, 937 (2004).